frontiers | Frontiers in Physics

TYPE Brief Research Report
PUBLISHED 15 December 2023
DOI 10.3389/fphy.2023.1303690

OPEN ACCESS

EDITED BY
Thomas Beyer,
Medical University of Vienna, Austria

REVIEWED BY
Siddesh V. Hartimath,
Institute of Bioengineering and Bioimaging (IBB), A*STAR, Singapore
Roberto Francischello,
University of Pisa, Italy

*CORRESPONDENCE
Thomas Wanek,
thomas.wanek@meduniwien.ac.at

RECEIVED 28 September 2023
ACCEPTED 20 November 2023
PUBLISHED 15 December 2023

CITATION
Wanek T, Mairinger S, Filip T, Löbsch M, Stanek J and Kuntner C (2023), Multi-organ comparison and quantification parameters of [18F]THK-5317 uptake in preclinical mouse models of tau pathology.
Front. Phys. 11:1303690.
doi: 10.3389/fphy.2023.1303690

Multi-organ comparison and quantification parameters of [^{18}F]THK-5317 uptake in preclinical mouse models of tau pathology

Thomas Wanek[1,2]*, Severin Mairinger[2,3], Thomas Filip[2,4], Mathilde Löbsch[2,5], Johann Stanek[1,2] and Claudia Kuntner[1,2,6]

[1]Department of Biomedical Imaging and Image-guided Therapy, Medical University of Vienna, Vienna, Austria, [2]Preclinical Molecular Imaging, AIT Austrian Institute of Technology GmbH, Seibersdorf, Austria, [3]Department of Clinical Pharmacology, Medical University of Vienna, Vienna, Austria, [4]Institute of Animal Breeding and Genetics and Biomodels Austria, University of Veterinary Medicine, Vienna, Austria, [5]Core Facility Laboratory Animal Breeding and Husbandry (CFL), Medical University of Vienna, Vienna, Austria, [6]Medical Imaging Cluster, Medical University of Vienna, Vienna, Austria

Introduction: Current small-animal PET instrumentation provides sufficient resolution, sensitivity, and quantitative accurate information on the radiotracer distribution within the whole body. However, most preclinical imaging studies focus on the disease-related organ of interest and do not use the total body information provided by small-animal PET. In this study, we investigated the distribution of [^{18}F]THK-5317 (also referred to as (*S*)-[^{18}F]THK-5117), a radiotracer initially developed to visualize tau deposits in the brain, in two transgenic mouse models of tau overexpression and littermate controls at different ages and of both sexes. We compared multiple quantitative parameters of radiotracer uptake in multiple organs of mice to investigate sex, age, or strain-related differences.

Methods: After intravenous administration, 60-min dynamic PET scans were acquired, followed by venous blood sampling, organ harvesting, and metabolite analysis by radio-thin-layer chromatography.

Results: Blood pharmacokinetics and metabolism of [^{18}F]THK-5317 significantly differed between males and females across all strains. Sex-related differences in organ V_Ts were identified from two-way ANOVA analysis. Organ-to-blood concentration ratios correlated well with organ V_Ts in all investigated organs.

Conclusion: Following our workflow, a straightforward multiple-organ analysis of [^{18}F]THK-5317 uptake in mice was easily achievable. From the derived quantitative parameters, the organ-to-blood values correlate best with the calculated V_Ts. Given the active incorporation of 3R principles into preclinical quantitative imaging, we propose that this workflow might be suitable to select novel radiotracer candidates before more complex kinetic models, comprising invasive methods such as full arterial blood sampling, for radiotracer quantification are applied.

KEYWORDS

[^{18}F]THK-5317, small-animal PET, tauopathy, sex-difference, tracer metabolism, brain uptake parameters

1 Introduction

Quantitative, non-invasive imaging technologies utilizing small laboratory animals are essential for research on the biodistribution of new drugs, disease progression, or response to novel therapeutic approaches. The availability of specifically bred or genetically modified mouse disease models, as well as technological advances in small-animal imaging instrumentation and methodologies, have led to significant discoveries on the molecular origins of these illnesses and triggered research on various novel therapeutic approaches [1–4].

Among the non-invasive imaging modalities, especially positron emission tomography (PET), utilizing radiolabeled compounds (radiotracers) offers considerable versatility in studying diseases from multiple perspectives and at different disease stages. Despite numerous species differences between rodents and humans, PET studies usually enable a high degree of translatability as many correlative and longitudinal study designs utilized in basic research can be modified to match current clinical safety requirements with reasonable effort [5–8].

Current small-animal PET instrumentation offers sufficient spatial resolution, high sensitivity for dynamic imaging, and, provided sufficient efforts are directed toward standardized protocols, a high degree of quantitative accuracy for rodent brain studies. Moreover, multimodal preclinical PET/CT scanners are available with an axial field of view (FOV) large enough to acquire whole-body mouse images in a single scan. As such, total-body positron emission tomography (TB-PET) scans, which are now increasingly emerging in clinical imaging, are easily achievable in mice. Such total-body scans provide holistic and dynamic information on radiotracer distribution within the scanned subject during the whole acquisition time. However, most preclinical imaging studies only focus on the disease-related organ of interest and do not use total body information. This is especially true for neurological diseases or disorders, where the brain is the focus [9–13].

TB-PET enables the quantification of radiotracer pharmacokinetics throughout the entire body or multiple organ systems in a single scan acquisition. These data form the basis for subsequent kinetic modeling where the distribution of radioactivity in the target organ and the input function (the time course of the radiotracer in the blood or plasma) are used to determine the local tissue concentration(s). Further graphical evaluation methods to quantify the organ uptake in terms of the distribution volume (V_T) provide non-invasive, quantitative measures that can then be observed in a systems biology approach [14–17].

The challenge in using whole-organ (blood/plasma-based) kinetic modeling in small-animal imaging lies in the requirement for an arterial blood input function and the determination of radioactive metabolites. In mice, however, arterial blood sampling is often impossible and limited by the small total blood volume. Even when arterial blood sampling is performed, the study design is limited to non-recovery imaging procedures, rendering longitudinal studies in aged animals or comparative studies of different therapeutic interventions in the same animal impossible. Closed-loop systems to avoid blood loss during such imaging procedures require long pre-scan preparation times, surgically skilled personnel, and are not feasible in a high-throughput manner [18]. Alternatively, a whole-blood based, non-invasive image-derived input function (IDIF), derived from small-animal total-body images, can be obtained, an approach that has been shown to be feasible in multiple preclinical radiotracer evaluations [19]. Using modern small-animal PET scanners, IDIF can be accurately derived by measuring the time–radioactivity concentration curves (TACs) in the left ventricle or a major vessel in mice [20]. For certain radiotracers, using population-based IFs and metabolization data has shown to be feasible in rodents [21–23].

Another aspect of adding total body information to small-animal PET might be the identification of sex differences in radiotracer pharmacokinetics, response to therapies, or metabolic changes during disease progression. Consequently, putative sex differences may be identified and addressed accordingly. It is commonly recognized that organ size and function change during aging and are sex-dependent. However, such differences are not reflected by changes in the whole-body weight of the respective animals [24]. This is particularly relevant for the excretory organs such as the liver and the kidneys, which directly influence radiotracer metabolism and elimination kinetics.

We recently reported one such sex difference in an APP/h Tau rat model so far as the plasma pharmacokinetics and metabolism of the putative tau radiotracer [^{18}F]THK-5317 (also referred to as (*S*)-[^{18}F]THK-5117) were different between male and female rats [22].

In the present study, our goal is to investigate the multi-organ distribution of [^{18}F]THK-5317 in the brain and peripheral tissues in two transgenic mouse models of tau overexpression, as well as their littermate controls, across various age groups and both sexes. Peripheral tau accumulation has been reported recently and has not yet been explored with dynamic PET [25,26]. We further aim to introduce a systematic workflow for performing quantitative analysis on multiple organs in mice. Lastly, we compared different quantification measures other than the Logan volume of distribution (V_T) as outcome parameters for [^{18}F]THK-5317 uptake.

2 Materials and methods

2.1 Chemicals

Chemicals were purchased from Sigma-Aldrich Handels GmbH (Vienna, Austria) and used without further purification. Radiosynthesis of [^{18}F]THK-5317 was performed, following the established protocols [22,27]. For this study, [^{18}F]THK-5317 (n = 15) was synthesized with a decay-corrected radiochemical yield of 12% ± 4% and a radiochemical purity of 95% ± 3% in a synthesis time of 76 ± 4 min. Molar activity at the end of synthesis was 498 ± 281 GBq/μmol.

2.2 Animals

We examined hTau (B6.Cg-*Mapt*$^{tm1(EGFP)Klt}$ Tg(MAPT)8cPdav/J) [28] and TMHT (Thy-1-mutated human tau) [29], as well as non-transgenic hTau littermates (as ntg-control), in this study. In total, 86 mice purchased from QPS Austria GmbH (Grambach, Austria) were used. Mice were scanned at 20, 44, or 68 weeks of age, including both sexes. A detailed study summary is provided in Supplementary

Table S1. Mice were housed in a temperature- and humidity-controlled facility under a cycle of 12/12 h of light/dark with free access to standard laboratory animal diet (ssniff R/M-H, ssniff Spezialdiäten GmbH, Soest, Germany) and water *ad libitum*. An acclimatization period of at least 1 week was allowed before animals were used in the experiments. Of the 86 mice, 14 mice, especially of the 44- and 68-week age groups, were lost during imaging (e.g., technical problems with the scanner and breathing arrest under anesthesia while scanning), yielding 72 PET datasets available for analysis. In one mouse, blood sampling and tissue harvesting were not possible. The study was approved by the national authorities (LF1-TVG-48/028-2016; Amt der Niederösterreichischen Landesregierung, Austria), and study procedures followed the European Communities Council Directive 2010/63/EU. The animal experimental data reported in this study comply with the ARRIVE (Animal Research: Reporting of *in Vivo* Experiments) guidelines 2.0 [30].

2.3 Small-animal PET imaging

PET imaging was performed on a small-animal PET scanner (Focus 220™, Siemens Healthineers, Knoxville, TN, United States) with 7.6 cm axial and 19 cm transaxial field-of-view [31]. Two mice (side by side) were imaged during one PET acquisition using a dual-mouse imaging cradle (m2m Imaging Corp, Cleveland, OH, United States). Before initiating PET acquisitions, anesthesia was induced in an induction box with isoflurane [concentration: 1.5%–3.0% (v/v)] in medical air as carrier gas. Afterward, animals were positioned on the dual-mouse imaging cradle, and isoflurane concentration levels were adjusted [range: 0.8%–1.5% (v/v)] to maintain the respiratory rate of the animals between 60 and 80 breaths/minute during the scan procedure. Then, the lateral tail veins were catheterized after warming the tails using pre-heated (~38°C) pads. Animals were warmed throughout the experiment, and the body temperature and respiratory rate were constantly monitored (SA Instruments Inc., Stony Brook, NY, United States). All animals underwent a 60-min dynamic [^{18}F]THK-5317 scan. Data acquisition was initiated at the start of intravenous injection (0.15 mL as slow bolus over ~ 40 sec), and list-mode data were acquired with an energy window of 250–750 keV and a 6-ns timing window. A 10-min transmission scan was performed using a rotating ^{57}Co-point source before each PET scan for attenuation correction. At the end of the scan, a blood sample was collected into a small tube (Microvette CB 300 LH, Sarstedt AG & Co, Nümbrecht, Germany) by puncture of the retrobulbar plexus, and animals were euthanized by cervical dislocation under deep anesthesia. Afterward, the organs of interest were extracted for gamma counting.

2.4 *Ex vivo* analysis of samples

Blood was centrifuged to obtain plasma (17,000 g, 4°C, 1 min), and radioactivity concentrations in blood, plasma samples, and organs were measured in a gamma counter (HIDEX AMG automatic gamma counter, Turku, Finland). Data from the gamma counter were decay-corrected to the time of radiotracer injection. Then, data were corrected by animals' injected activity, and expressed as percentage of injected dose per gram (%ID/g). Individual plasma-to-blood concentration ratios (P/B ratio) at 60 min after [^{18}F]THK-5317 administration were calculated by dividing the radioactivity concentration measured in the plasma by the radioactivity measured in the blood of the respective animal.

2.5 Metabolite analysis

The percentage of unchanged (unconjugated) [^{18}F]THK-5317 was analyzed by radio-thin-layer chromatography (radio-TLC). Blood was centrifuged to obtain plasma, and proteins were precipitated with acetonitrile (1 µL per µL plasma). Tissues were homogenized using an Ultra Turrax T10 instrument (IKA Laboratory Equipment, Staufen, Germany), and proteins were precipitated with acetonitrile (0.2 mL per brain). All solutions were vortexed and centrifuged (12,000 × g, 1 min, 21°C). Approximately 5 µL of the supernatant and diluted radiotracer solution as references were spotted on silica gel 60F 254-nm TLC plates (10 × 20 cm; Merck, Darmstadt, Germany), and plates were developed in dichloromethane/methanol (95/5, v/v). Detection was performed by exposing the TLC plates to multi-sensitive phosphor screens overnight. The screens were then scanned at 300 dpi resolution using a phosphor imager (Cyclone® Plus, PerkinElmer, Waltham, MA, United States). The retardation factor (Rf) of [^{18}F]THK-5317 was 0.58, as assessed using unlabeled reference standards.

2.6 PET image analysis

Dynamic list-mode data from the 60-min scans were sorted into three-dimensional sinograms, according to the following frame sequence: 8 × 5 s, 2 × 10 s, 2 × 30 s, 3 × 60 s, 2 × 150 s, 2 × 300 s, and 4 × 600 s. PET images were reconstructed by Fourier rebinning of 3D sinograms, followed by two-dimensional filtered back projection with a ramp filter, resulting in a voxel size of 0.4 × 0.4 × 0.8 mm^3. The standard data correction protocol was applied to the data, including normalization, attenuation, and decay correction. Before each measurement series, the PET scanner was cross-calibrated with the activimeter by imaging a phantom with a known activity concentration of an ^{18}F-radiotracer solution.

On the dynamic PET images, organs of interest (the brain, heart, lung, liver, left kidney, and muscle) were defined by delineating pre-defined volumes of interest (VOIs) using the software program AMIDE [32]. Then, TACs of these VOIs were extracted, and the area under the curves (AUCs) from 0 to 60 min were calculated.

The heart curve was used as an IDIF. First, the heart curve was scaled to the blood curve using the blood activity from the gamma counter. Then, a sex-specific (male or female) plasma-to-blood ratio (P/B ratio) was applied to obtain the plasma input function. For metabolite correction, a simple linear regression was performed, assuming a parent fraction of 1 (100%) at 0 s and the measured parent fraction at 3,600 s, separate for the male and female animals. The sex-specific plasma input function was then corrected by the resulting linear equation. The final obtained metabolite-corrected plasma input function $C_p(t)$ was used for calculating the volumes of

distribution (V_T) for different organs derived from the slope of the linearized Logan graphical analysis [33]:

$$\frac{\int_0^T C_{ROI}(t)dt}{C_{ROI}(T)} = V_T \times \frac{\int_0^T C_p(t)dt}{C_{ROI}(T)} + Int,$$

where AUC_{ROI} for each organ from 0-T was used as a measure of $\int_0^T C_{ROI}(t)dt$. For all assessed organs, the plot became linear after 10 min.

In addition, radiotracer clearance from the plasma was performed on decay- and metabolite-corrected plasma radioactivity data from all animals. Plasma clearance was calculated as the quotient of the injected activity divided by the AUC and corrected by the body weight of the animal [34]:

$$Clearance\left[mL/h/g\,BW\right] = \frac{Inj\,Activity\left[kBq\right]}{AUC\left[\frac{kBq}{mL}*h\right]} * BW^{-1}\left[g^{-1}\right].$$

Moreover, we calculated the organ-to-blood ratio by dividing the organ activity values derived from the last PET frame (50–60 min) by the corresponding blood activity values measured with the gamma counter of the respective animal.

2.7 Statistics

Statistical testing was performed using GraphPad Prism 9.1.0 software (GraphPad Software, La Jolla, CA, United States). Differences between groups were analyzed by two-way ANOVA using a full model for assessing the effects of sex, strain and age, and the interaction between them, followed by Tukey's multiple comparison test. Alternatively, two-tailed, unpaired t-tests were used to compare groups in the biodistribution experiments. The level of statistical significance was set to $p < 0.05$. Unless stated otherwise, all values are given as mean ± standard deviation (SD).

3 Results

VOI-based analysis of the dynamic small-animal PET data was performed to determine the brain, liver, lung, kidney, and muscle retention of [^{18}F]THK-5317. PET images, as well as the derived organ TACs for the investigated mouse strains, are shown in Supplementary Figures S1–S7. In all investigated organs, [^{18}F]THK-5317 showed a peak uptake within the first 5–10 min after intravenous administration, followed by a fast washout from the organs until the end of the PET scan. The highest organ uptake (%ID/g) was observed in the liver and kidney, followed by the lungs and brain, and was lowest in muscle tissue. No distinct differences in radiotracer pharmacokinetics were observed in TACs, irrespective of the mouse strain, age group, and sex, except for the kidney.

Biodistribution performed at the end of the PET scans showed no significant age dependency of [^{18}F]THK-5317 uptake in the investigated organs (Supplementary Tables S2–S4). Data from different age groups within the investigated mouse strains were pooled to further focus on sex-related issues. After data pooling, blood pharmacokinetics of [^{18}F]THK-5317 showed significant differences between male and female individuals across all strains (Table 1). In general, female mice showed higher blood radioactivity at 60 min after radiotracer injection (0.50 ± 0.21; 0.43 ± 0.15; 0.36 ± 0.09 %ID/g in ntg-control, hTau, and TMHT mice, respectively) compared to male mice (0.29 ± 0.15; 0.25 ± 0.08; 0.27 ± 0.07 %ID/g in ntg-control, hTau, and TMHT mice). In addition, in plasma, female mice showed higher radioactivity concentration levels at 60 min after radiotracer injection (0.62 ± 0.25; 0.51 ± 0.01; 0.50 ± 0.13 %ID/g in ntg-control, hTau, and TMHT mice, respectively) when compared to male mice (0.45 ± 0.24; 0.37 ± 0.12; 0.35 ± 0.09 %ID/g in ntg-control, hTau, and TMHT mice). The derived plasma/blood ratios at 60 min, however, were not different between males and females. Radiotracer clearance from plasma was not significantly different between the investigated age, strain, or sex groups (Supplementary Figure S8). Further significant sex-related uptake differences were found for the liver, which was higher in female ntg-control (2.39 ± 0.92 vs. 1.33 ± 0.65 %ID/g) and hTau (2.53 ± 1.53 vs. 1.52 ± 0.41 %ID/g) mice but lower in TMHT mice (0.26 ± 0.36 vs. 0.93 ± 0.69 %ID/g) compared to male mice. Additional significant differences in the organ uptake between male and female ntg-control and hTau mice but not in TMHT mice were found in the urinary bladder and bone (*Os femoris*) (Table 1).

For the plasma and brain, no significant differences in metabolism of [^{18}F]THK-5317 were identified between ntg-control, hTau, and TMHT mice, regardless of age. However, a trend of more extensive metabolism in female compared to male mice was observed (Supplementary Table S5). When pooled, female mice showed a significantly higher fraction of radiometabolites of [^{18}F]THK-5317 in plasma (22.1% ± 5.9% unchanged parent) compared to male mice (26.0% ± 7.7% unchanged parent). Additionally, in some animals, liver metabolization of [^{18}F]THK-5317 was assessed, showing a higher fraction of radiometabolites (2.2% ± 0.6% vs. 3.9% ± 1.9% unchanged parent) in female vs. male mice. In the brain, the percentage of the unchanged radiotracer did not differ between female and male mice (Table 2). For the determination of brain V_Ts as the outcome parameter for [^{18}F]THK-5317 distribution, we generated an image-derived blood input function (IDIF) by placing a spherical VOI over the heart of the individual animals. For validation, we compared such derived PET blood radioactivity measurements in the last PET frame (50–60 min after radiotracer administration) with the radioactivity measured in the venous blood sample taken at the end of the PET scan in the gamma counter. In line with our previous experiences [35], heart radioactivity concentrations measured in PET showed a good correlation with the respective gamma counter values ($r = 0.704$, $p < 0.0001$, Supplementary Figure S9).

Based on individual blood IDIFs and the population-based metabolite correction, we derived the organ uptake of [^{18}F]THK-5317, expressed as Logan V_T in the investigated mouse groups (Figure 1). In the brain, two-way ANOVA analysis revealed a statistically significant effect of sex on brain V_Ts ($F_{1,54} = 7.462$, $p = 0.009$, $\eta^2 = 0.123$) and an effect of strain and age ($F_{8,54} = 3.302$, $p = 0.004$, $\eta^2 = 0.333$). In contrast, in the liver, no significant effect between the investigated study groups was found. Further significant sex-related differences in organ V_Ts were identified from the two-way ANOVA analysis in the lung ($F_{1,54} = 4.662$, $p = 0.035$, $\eta^2 = 0.079$), kidney ($F_{1,54} = 16.52$, $p = 0.002$, $\eta^2 = 0.169$), and muscle

TABLE 1 Biodistribution of [^{18}F]THK-5317 in male and female (pooled over the investigated age groups) non-transgenic hTau littermates (ntg-control), hTau (B6.Cg-Mapt$^{tm1(EGFP)Klt}$ Tg(MAPT)8cPdav/J), and TMHT (Thy-1 mutated human tau) mice obtained at 60 min after intravenous administration. Data are presented as mean percent of injected dose per gram tissue (%ID/g) ± standard deviation. Significance indicates differences between male and female individuals of the respective study groups.

Study group	ntg-control			hTau			TMHT		
	Male	*Female*	*Significant**	*Male*	*Female*	*Significant**	*Male*	*Female*	*Significant**
	n = 11	*n = 11*		*n = 13*	*n = 11*		*n = 11*	*n = 14*	
Blood	0.29 ± 0.15	0.50 ± 0.21	*p = .004*	0.25 ± 0.08	0.43 ± 0.15	*p = .028*	0.27 ± 0.07	0.36 ± 0.09	*p = .011*
Plasma	0.45 ± 0.24	0.62 ± 0.25	*p = .031*	0.37 ± 0.12	0.51 ± 0.1	*p = .033*	0.35 ± 0.09	0.50 ± 0.13	*p = .003*
Brain	0.27 ± 0.08	0.29 ± 0.14	*n.s.*	0.24 ± 0.10	0.24 ± 0.06	*n.s.*	0.24 ± 0.09	0.28 ± 0.09	*n.s.*
Heart	0.34 ± 0.13	0.47 ± 0.15	*n.s.*	0.39 ± 0.17	0.38 ± 0.04	*n.s.*	0.32 ± 0.08	0.37 ± 0.08	*n.s.*
Lung	0.52 ± 0.22	0.68 ± 0.25	*n.s.*	0.67 ± 0.32	0.54 ± 0.22	*n.s.*	0.53 ± 0.15	0.55 ± 0.13	*n.s.*
Liver	1.33 ± 0.65	2.39 ± 0.92	*p = .011*	1.52 ± 0.41	2.53 ± 1.53	*p = .044*	0.93 ± 0.69	0.26 ± 0.36	*p = .028*
Kidney	0.72 ± 0.26	0.86 ± 0.26	*n.s.*	0.88 ± 0.33	0.77 ± 0.15	*n.s.*	1.25 ± 0.89	0.95 ± 0.28	*n.s.*
Spleen	0.52 ± 0.22	0.52 ± 0.13	*n.s.*	0.53 ± 0.27	0.67 ± 0.42	*n.s.*	1.33 ± 0.79	1.40 ± 0.78	*n.s.*
Stomach	2.07 ± 1.44	2.25 ± 1.37	*n.s.*	2.39 ± 1.34	1.46 ± 0.24	*n.s.*	2.12 ± 0.88	1.52 ± 0.41	*n.s.*
Small intestine	2.37 ± 1.64	2.36 ± 1.53	*n.s.*	5.46 ± 5.20	3.58 ± 2.5	*n.s.*	-	-	-
Large intestine	0.82 ± 0.36	1.17 ± 0.38	*n.s.*	1.49 ± 2.28	0.89 ± 0.21	*n.s.*	1.48 ± 0.65	1.24 ± 0.36	*n.s.*
Gall bladder	83.08 ± 50.6	83.57 ± 61.02	*n.s.*	102.77 ± 83.78	58.69 ± 58.09	*n.s.*	80.27 ± 79.87	41.76 ± 44.19	*n.s.*
Urine	17.74 ± 13.5	21.11 ± 20.93	*n.s.*	15.89 ± 10.39	10.47 ± 5.51	*n.s.*	17.00 ± 18.69	19.72 ± 12.95	*n.s.*
Urinary bladder	5.21 ± 1.54	1.25 ± 0.78	*n.s.*	6.22 ± 2.38	3.39 ± 1.58	*p = .021*	6.02 ± 3.37	5.24 ± 3.34	*n.s.*
Bone	*0.33 ± 0.12*	0.15 ± 0.11	*p = .008*	0.20 ± 0.12	0.19 ± 0.08	*p = .044*	0.22 ± 0.06	0.20 ± 0.04	*n.s.*
Muscle	*0.26 ± 0.08*	0.30 ± 0.13	*n.s.*	0.23 ± 0.09	0.22 ± 0.05	*n.s.*	0.21 ± 0.05	0.23 ± 0.06	*n.s.*

*Statistical significance was determined using a two-tailed, unpaired t-test. The level of significance was set to $p < 0.05$. n.s. : not significant.

TABLE 2 Levels of the unchanged parent of [^{18}F]THK-5317 determined at 60 min after radiotracer injection in male and female individuals of the investigated mouse study groups. Data show pooled values for male and female individuals, irrespective of the age group or strain.

Study group			
	Male	*Female*	*Significant**
	n = 35	*n = 36*	
Plasma	26.00 ± 7.67	22.08 ± 5.94	*p = .032*
Brain	47.26 ± 12.35	48.90 ± 11.77	*n.s.*
Liver	3.86 ± 1.94 #	2.19 ± 0.60 #	*p = .020*

the number was lower for the liver analysis; *n* = 8 for male and *n* = 10 for female.
Statistical significance was determined using a two-tailed, unpaired t-test. The level of significance was set to $p < 0.05$. n.s. : not significant.

($F_{1,54} = 4.923$, $p = 0.031$, $\eta^2 = 0.084$). Alternative organ analysis given as organ-to-blood ratios revealed similar effects of sex in the identical organs such as the brain/blood ($F_{1,54} = 12.02$, $p = 0.001$, $\eta^2 = 0.182$), lung/blood ($F_{1,54} = 13.37$, $p = 0.001$, $\eta^2 = 0.198$), kidney/blood ($F_{1,54} = 6.399$, $p = 0.014$, $\eta^2 = 0.106$), and muscle/blood ($F_{1,54} = 8.052$, $p = 0.006$, $\eta^2 = 0.130$) but not in the liver/blood ($F_{1,54} = 0.562$, $p = 0.457$). Interestingly, organ AUC values exhibited a significant effect of sex on the brain ($F_{1,54} = 12.68$, $p = 0.0008$, $\eta^2 = 0.190$), liver ($F_{1,54} = 42.29$, $p < 0.0001$, $\eta^2 = 0.439$), and lung ($F_{1,54} = 9.482$, $p = 0.033$, $\eta^2 = 0.149$) but not on the other organs. The individual organ AUC values, as well as organ-to-blood ratios for ntg-control, hTau, and TMHT mice, are shown in Supplementary Figures S10, S11. Individual comparisons obtained with Tukey's multiple comparisons test showed significant differences between certain individual groups for some organs (e.g., the kidney). However, these differences did not follow a general trend and varied between the organs.

Correlation analysis of different organ uptake measures of [^{18}F]THK-5317 such as AUC_{organ}, organ-to-blood ratio, and measured concentration in the last PET frame (%ID/g) to the respective V_Ts is shown in Figure 2. Organ-to-blood ratios showed a statistically significant correlation to the respective organ V_Ts for all analyzed

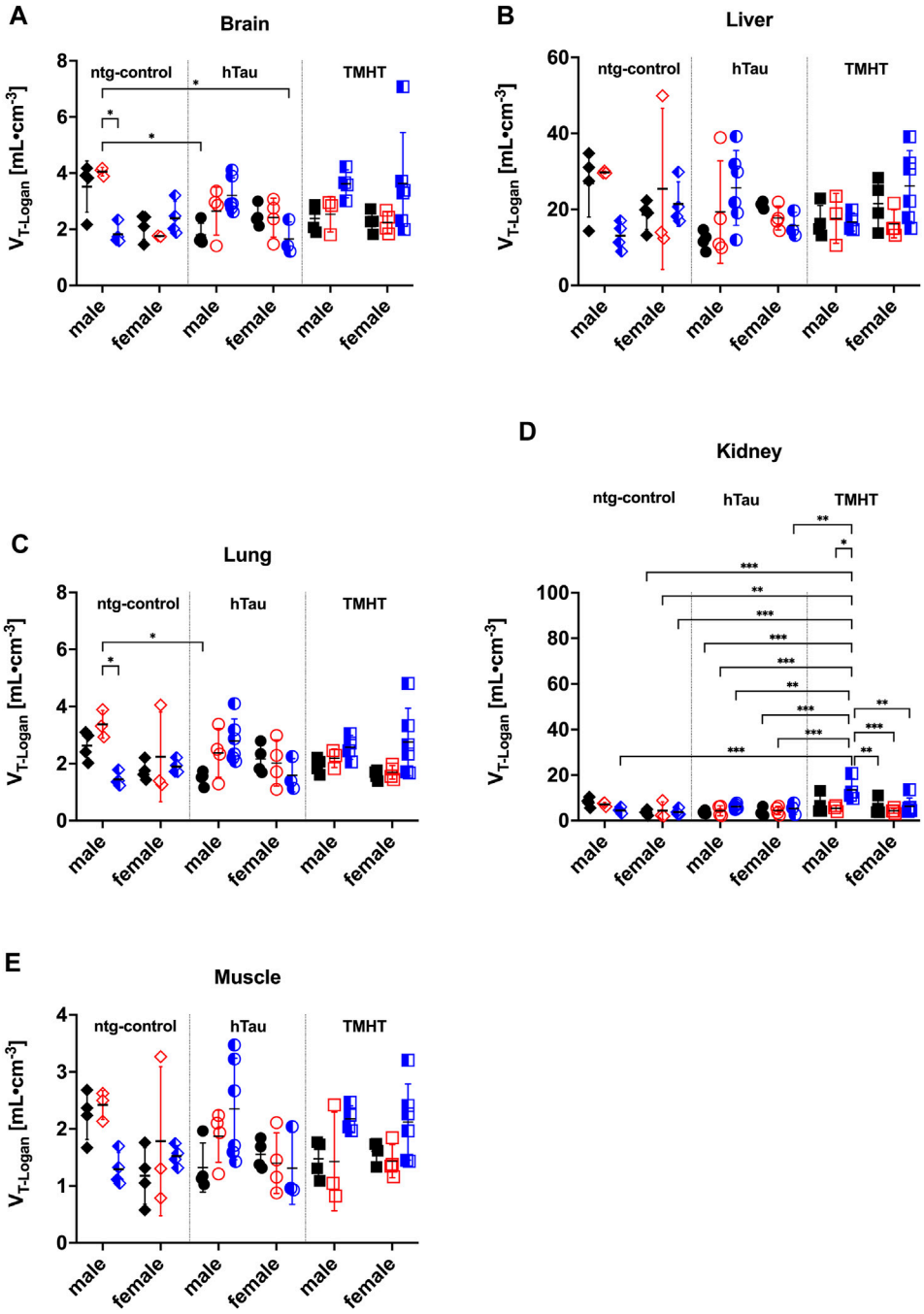

FIGURE 1
Whole-organ volume of distribution (V_T) of [^{18}F]THK-5317 obtained with Logan graphical analysis in the **(A)** brain, **(B)** liver, **(C)** lung, **(D)** kidney, and **(E)** muscle in male and female non-transgenic hTau littermates (ntg-control), hTau (B6.Cg-Mapt$^{tm1(EGFP)Klt}$ Tg(MAPT)8cPdav/J), and TMHT (Thy-1 mutated human tau) mice aged 20 weeks (black, closed symbols), 44 weeks (red, open symbols), and 68 weeks (blue, half-open symbols). *$p < 0.05$, **$p < 0.01$, and ***$p < 0.001$; two-way ANOVA followed by Tukey's multiple comparison test.

organs: the brain ($r = 0.707$, $p < 0.0001$), liver ($r = 0.798$, $p < 0.0001$), lung ($r = 0.751$, $p < 0.0001$), kidney ($r = 0.337$, $p = 0.0038$), and muscle ($r = 0.679$, $p < 0.0001$). In addition, a positive correlation between kidney V_T and AUC_{kidney} ($r = 0.4655$, $p < 0.0001$), and kidney %ID/g at 60 min after radiotracer administration ($r = 0.2527$, $p = 0.0322$) was identified.

4 Discussion

We were interested in identifying the sex, age, or strain-related differences in the distribution and kinetics of tau-radiotracer [^{18}F] THK-5317 on a whole-organ level. We, therefore, quantitatively analyzed PET images obtained in three different mice strains at three

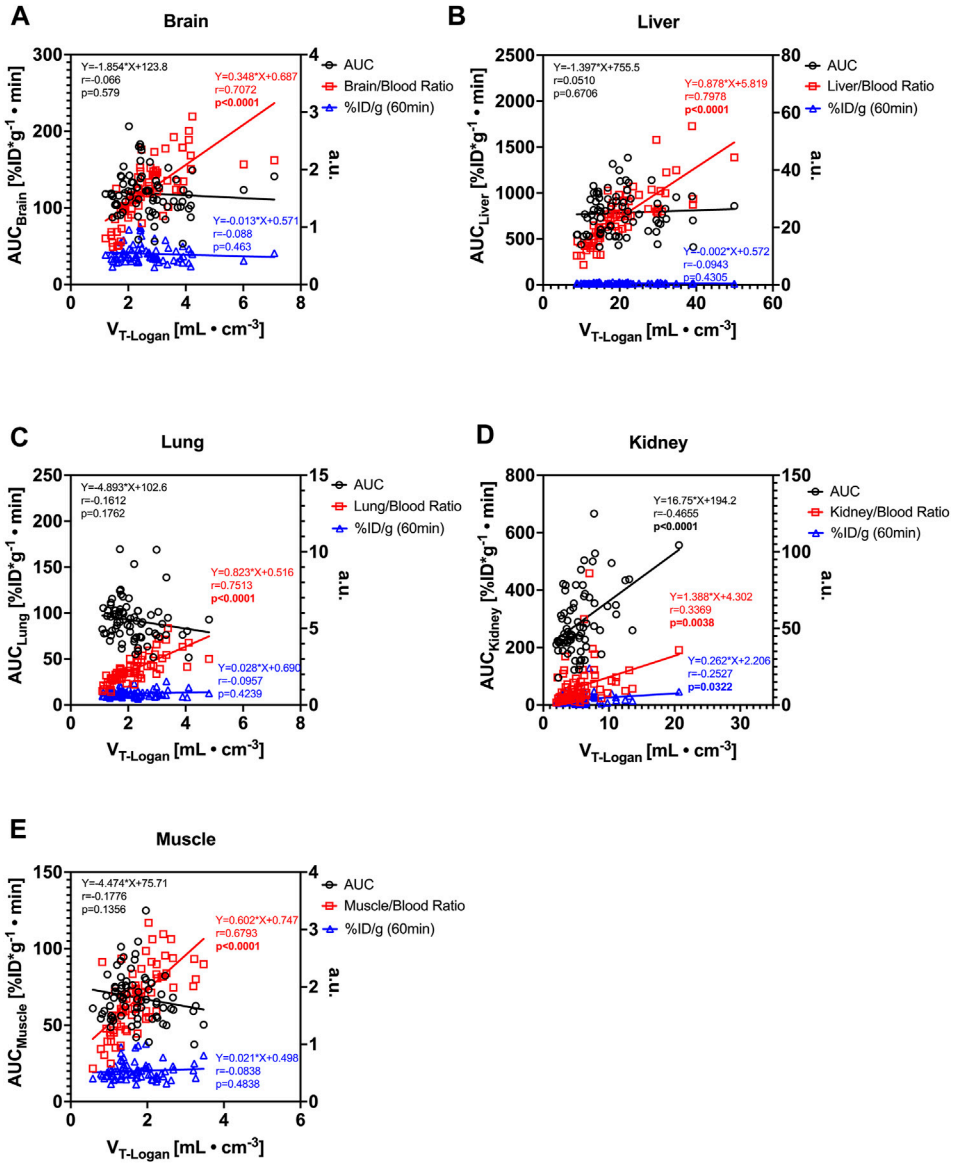

FIGURE 2
Comparison of measures of the [^{18}F]THK-5317 uptake in the **(A)** brain, **(B)** liver, **(C)** lung, **(D)** kidney, and **(E)** muscle and correlation analysis of whole-organ area under the concentration curve (AUC_{Organ}), organ-to-blood ratio at the end of the PET scan, and PET-derived percent of injected dose per gram tissue (%ID/g) at 60 min after the administration with the volume of distribution (V_T) obtained with Logan graphical analysis. (a.u. = arbitrary units either %ID/g or organ-to-blood ratio; *r* = Pearson correlation coefficient; p = *p*-value for Pearson correlation; linear regression formula shows the slope and intercept of the respective simple linear regression fit.)

different ages using both sexes in terms of percent of injected dose per gram tissue (%ID/g). Moreover, we were interested if alternative quantitative parameters such as AUC values, or organ-to-blood ratios, which are easier to obtain in mice, can be used as a surrogate for the volume of distribution (V_T) obtained by Logan graphical analysis. In line with previous observations in rats [22], we observed sex-related differences in the [^{18}F]THK-5317 uptake in the studied mice. In all strains, we observed significant differences in blood and plasma uptake between male and female mice. Contrary to rats, in the studied mice, the female values were overall higher. Biodistribution values agree with values published previously by [36] in male ICR mice. Apart from blood and plasma, we additionally obtained a sex-related difference in the liver (all strains), bone (ntg-control and hTau), and urinary bladder (hTau).

It is broadly recognized that drug pharmacokinetics are largely affected by hepatic drug-metabolizing enzymes (DME) and that their function is highly variable between species, strains, and sex [37]. Our observation suggests different retention/metabolization of [^{18}F]THK-5317 in these animals by phase I/II DME or other DME-regulating factors. Interestingly, in the liver, [^{18}F]THK-5317 uptake was higher in female ntg-control and hTau mice compared to male mice, whereas in TMHT mice, it was the opposite. As ntg-control and hTau mice share an identical genetic background in contrast to TMHT mice, the probable involvement of additional strain-dependent co-factors in

DME expression and function is likely. We, therefore, speculate that the differences observed in this study are related to sex- and strain-dependent hepatic processes which require further studies.

Surprisingly, we obtained a small but statistically higher amount of unchanged parent at 60 min post-injection in plasma in male mice (26%) compared to female mice (22%). Irrespective of sex, the obtained values were in good agreement with values reported in other mouse strains [38]. Yet, the unchanged parent in the brain was comparable between the sexes (47% male vs. 49% female), and the obtained values were significantly lower than that reported by Alzghool et al. (95% unchanged parent in the brain tissue of APP/PS1-21 mice), as well as our findings in rats at the same sampling time [22]. These findings emphasize the importance of radiometabolite analysis within the respective study setup and that the rate of tracer metabolism can differ not only between species but also between individual mouse strains. Furthermore, this supports our previous observations [22] showing that mice seem to metabolize [^{18}F]THK-5317 much faster than rats.

Whole-organ V_Ts of [^{18}F]THK-5317 were highest for the liver, followed by the kidney, brain, lung, and muscle. The rank order of organ V_Ts generally followed previous reports on tau retention, but further correlation studies are required [26].

Our attempt to identify an alternative approach to derive alternative quantitative parameters has shown that the organ-to-blood values exhibited the best correlation to the calculated V_Ts. This is not surprising as both parameters are based on organ-to-blood activity ratios. Yet, we believe that this approach might be a good base for the evaluation of new radiotracers as blood samples at the end of the PET scan are easy to obtain. In addition, it also offers the possibility to examine plasma and radioactive metabolites. When a new radiotracer shows promising parameters using this approach, a more complex kinetic model and specifically a full arterial IF could be planned for subsequent preclinical evaluation. This strategy might aid in decreasing severity and the number of research animals used, and further facilitates candidate selection, following this low-complexity setup in preclinical PET studies.

However, we have identified the following limitations from our study. First, [^{18}F]THK-5317 is metabolically unstable, not exclusively tau-selective, and has been shown to bind to Aß plaques and monoamine oxidase B (MAO-B) in mouse models [38,39]. Although hTau and TMHT mice used in this study clearly showed the absence of ß-amyloid, cerebral MAO-B expression has not been investigated. Furthermore, MAO-B expression increases as part of the neuroinflammatory response to tau accumulations, as well as during aging [40,41]. It cannot be excluded that the sex differences identified in the whole-brain uptake of [^{18}F]THK-5317 solely reflects changes in MAO-B expression patterns as sex-dependency of MAO-isoform expression has been confirmed in the human brain [42]. Second, our initial assumption about the estimated effect size for sample size calculation for different study groups was incorrect. We, therefore, pooled the acquired data over age and strain groups to increase the respective group sizes, which ultimately revealed statistically significant differences. Conclusively, this study highlights the importance of preliminary, pilot studies from which effect sizes and, ultimately, sample size calculations can be based on real-world data obtained in the own research environment and not solely based on the published data. Third, the heart input function suffered from spillover from the liver and gall bladder signals, especially in the late time frames. We, therefore, carefully positioned the heart VOI to minimize this influence. Fourth, for the calculation of the liver V_T, we only used a single input function and did not account for the dual blood supply (the portal vein and the hepatic artery). In PET-only images without anatomical guidance, the liver portal vein cannot be identified in mice. Fifth, the IDIF method was not validated to the ground truth, which would be the arterial sampling. This might add some additional bias to the results. Finally, the radiosynthesis process of [^{18}F]THK-5317 requires further optimization to consistently achieve radiochemical purities above 98%.

In conclusion, we presented a workflow for quantitative, multiple-organ analysis of the [^{18}F]THK-5317 uptake in mice, revealing sex-differences in the plasma concentration, the formation of radiometabolites, and uptake in various organs in mice. From the derived quantitative parameters, the organ-to-blood values correlate best with the calculated V_Ts. Given the active incorporation of 3R principles into preclinical quantitative imaging, we propose that following this workflow, comprising dynamic PET scans, concomitant blood sampling, subsequent metabolite analysis, and candidate selections based on organ-to-blood uptake parameters, might be suitable to select novel radiotracer candidates before more complex kinetic models, comprising invasive methods such as full arterial blood sampling, for radiotracer quantification are applied.

Data availability statement

The raw data supporting the conclusion of this article will be made available by the authors, without undue reservation.

Ethics statement

The animal study was approved by Intramural Committee for Animal Experimentation. The study was conducted in accordance with the local legislation and institutional requirements.

Author contributions

TW: conceptualization, formal analysis, investigation, methodology, project administration, resources, writing–original draft, and visualization. SM: conceptualization, investigation, and writing–review and editing. TF: conceptualization, investigation, methodology, project administration, and writing–review and editing. ML: investigation, methodology, and writing–review and editing. JS: investigation and writing–review and editing. CK: conceptualization, data curation, funding acquisition, methodology, project administration, resources, visualization, and writing–original draft.

Funding

The author(s) declare that financial support was received for the research, authorship, and/or publication of this article. Methodology used for research leading to these results has received funding from

the Austrian Research Promotion Agency (FFG) through project number 853256 awarded to CK.

Acknowledgments

The authors would like to acknowledge the efforts of the management teams at the Medical University of Vienna and at the AIT Austrian Institute of Technology GmbH to enable the successful transfer of the former AIT Preclinical Molecular Imaging Group to the Medical University of Vienna. The authors would also like to thank Michael Sauberer and Sarah Furtner for their help in conducting the experiments and analyzing data. We further thank our colleagues from Radiopharmaceuticals, Seibersdorf Labor GmbH, for their continuous support.

Conflict of interest

Authors TW, SM, TF, ML, JS, and CK were employed by AIT Austrian Institute of Technology GmbH.

The author(s) declared that they were an editorial board member of Frontiers, at the time of submission. This had no impact on the peer review process and the final decision.

Publisher's note

Supplementary material

The Supplementary Material for this article can be found online at: https://www.frontiersin.org/articles/10.3389/fphy.2023.1303690/full#supplementary-material

References

1. Myers A, Mcgonigle P. Overview of transgenic mouse models for alzheimer's disease. *Curr Protoc Neurosci* (2019) 89:e81. doi:10.1002/cpns.81

2. Busche MA, Hyman BT. Synergy between amyloid-beta and tau in Alzheimer's disease. *Nat Neurosci* (2020) 23:1183–93. doi:10.1038/s41593-020-0687-6

3. Sanchez-Varo R, Mejias-Ortega M, Fernandez-Valenzuela JJ, Nunez-Diaz C, Caceres-Palomo L, Vegas-Gomez L, et al. Transgenic mouse models of alzheimer's disease: an integrative analysis. *Int J Mol Sci* (2022) 23:5404. doi:10.3390/ijms23105404

4. Chavan RS, Supalkar KV, Sadar SS, Vyawahare NS. Animal models of Alzheimer's disease: an origin of innovative treatments and insight to the disease's etiology. *Brain Res* (2023) 1814:148449. doi:10.1016/j.brainres.2023.148449

5. Cao L, Kong Y, Ji B, Ren Y, Guan Y, Ni R. Positron emission tomography in animal models of tauopathies. *Front Aging Neurosci* (2021) 13:761913. doi:10.3389/fnagi.2021.761913

6. Van Camp N, Lavisse S, Roost P, Gubinelli F, Hillmer A, Boutin H. TSPO imaging in animal models of brain diseases. *Eur J Nucl Med Mol Imaging* (2021) 49:77–109. doi:10.1007/s00259-021-05379-z

7. Chen B, Marquez-Nostra B, Belitzky E, Toyonaga T, Tong J, Huang Y, et al. PET imaging in animal models of alzheimer's disease. *Front Neurosci* (2022) 16:872509. doi:10.3389/fnins.2022.872509

8. Syvänen S, Meier SR, Roshanbin S, Xiong M, Faresjö R, Gustavsson T, et al. PET imaging in preclinical anti-aβ drug development. *Pharm Res* (2022) 39:1481–96. doi:10.1007/s11095-022-03277-z

9. Mannheim JG, Mamach M, Reder S, Traxl A, Mucha N, Disselhorst JA, et al. Reproducibility and comparability of preclinical PET imaging data: a multicenter small-animal PET study. *J Nucl Med* (2019) 60:1483–91. doi:10.2967/jnumed.118.221994

10. Herfert K, Mannheim JG, Kuebler L, Marciano S, Amend M, Parl C, et al. Quantitative rodent brain receptor imaging. *Mol Imaging Biol* (2020) 22:223–44. doi:10.1007/s11307-019-01368-9

11. Mcdougald W, Vanhove C, Lehnert A, Lewellen B, Wright J, Mingarelli M, et al. Standardization of preclinical PET/CT imaging to improve quantitative accuracy, precision, and reproducibility: a multicenter study. *J Nucl Med* (2020) 61:461–8. doi:10.2967/jnumed.119.231308

12. Miyaoka RS, Lehnert AL. Small animal PET: a review of what we have done and where we are going. *Phys Med Biol* (2020) 65:24TR04. doi:10.1088/1361-6560/ab8f71

13. Du J, Jones T. Technical opportunities and challenges in developing total-body PET scanners for mice and rats. *EJNMMI Phys* (2023) 10:2. doi:10.1186/s40658-022-00523-6

14. Patlak CS, Blasberg RG. Graphical evaluation of blood-to-brain transfer constants from multiple-time uptake data. Generalizations. *J Cereb Blood Flow Metab* (1985) 5:584–90. doi:10.1038/jcbfm.1985.87

15. Logan J, Fowler JS, Volkow ND, Wolf AP, Dewey SL, Schlyer DJ, et al. Graphical analysis of reversible radioligand binding from time-activity measurements applied to [N-11C-methyl]-(-)-cocaine PET studies in human subjects. *J Cereb Blood Flow Metab* (1990) 10:740–7. doi:10.1038/jcbfm.1990.127

16. Hood L, Heath JR, Phelps ME, Lin B. Systems biology and new technologies enable predictive and preventative medicine. *Science* (2004) 306:640–3. doi:10.1126/science.1104635

17. Innis RB, Cunningham VJ, Delforge J, Fujita M, Gjedde A, Gunn RN, et al. Consensus nomenclature for *in vivo* imaging of reversibly binding radioligands. *J Cereb Blood Flow Metab* (2007) 27:1533–9. doi:10.1038/sj.jcbfm.9600493

18. Alf MF, Wyss MT, Buck A, Weber B, Schibli R, Krämer SD. Quantification of brain glucose metabolism by 18F-FDG PET with real-time arterial and image-derived input function in mice. *J Nucl Med* (2013) 54:132–8. doi:10.2967/jnumed.112.107474

19. Bini J, Lattin CR, Toyonaga T, Finnema SJ, Carson R. Optimized methodology for reference region and image-derived input function kinetic modeling in preclinical PET. *IEEE Trans Radiat Plasma Med Sci* (2022) 6:454–62. doi:10.1109/trpms.2021.3088606

20. Lanz B, Poitry-Yamate C, Gruetter R. Image-derived input function from the vena cava for 18F-FDG PET studies in rats and mice. *J Nucl Med* (2014) 55:1380–8. doi:10.2967/jnumed.113.127381

21. Meyer M, Le-Bras L, Fernandez P, Zanotti-Fregonara P. Standardized input function for 18F-fdg PET studies in mice: a cautionary study. *PLoS One* (2017) 12:e0168667. doi:10.1371/journal.pone.0168667

22. Mairinger S, Filip T, Sauberer M, Flunkert S, Wanek T, Stanek J, et al. Plasma pharmacokinetic and metabolism of [(18)F]THK-5317 are dependent on sex. *Nucl Med Biol* (2020) 84-85:28–32. doi:10.1016/j.nucmedbio.2020.01.001

23. Filip T, Mairinger S, Neddens J, Sauberer M, Flunkert S, Stanek J, et al. Characterization of an APP/tau rat model of Alzheimer's disease by positron emission tomography and immunofluorescent labeling. *Alz Res Ther* (2021) 13:175. doi:10.1186/s13195-021-00916-2

24. Jin J, Yang X, Gong H, Li X. Time- and gender-dependent alterations in mice during the aging process. *Int J Mol Sci* (2023) 24:12790. doi:10.3390/ijms241612790

25. Gu Y, Oyama F, Ihara Y. Tau is widely expressed in rat tissues. *J Neurochem* (1996) 67:1235–44. doi:10.1046/j.1471-4159.1996.67031235.x

26. Solorzano A, Brady M, Bhatt N, Johnson A, Burgess B, Leyva H, et al. *Central and peripheral tau retention modulated by an anti-tau antibody* (2023). bioRxiv.

27. Tago T, Furumoto S, Okamura N, Harada R, Ishikawa Y, Arai H, et al. Synthesis and preliminary evaluation of 2-arylhydroxyquinoline derivatives for tau imaging. *J Labelled Comp Radiopharm* (2014) 57:18–24. doi:10.1002/jlcr.3133

28. Andorfer C, Kress Y, Espinoza M, De Silva R, Tucker KL, Barde YA, et al. Hyperphosphorylation and aggregation of tau in mice expressing normal human tau isoforms. *J Neurochem* (2003) 86:582–90. doi:10.1046/j.1471-4159.2003.01879.x

29. Flunkert S, Hierzer M, Löffler T, Rabl R, Neddens J, Duller S, et al. Elevated levels of soluble total and hyperphosphorylated tau result in early behavioral deficits and distinct changes in brain pathology in a new tau transgenic mouse model. *Neurodegener Dis* (2013) 11:194–205. doi:10.1159/000338152

30. Percie Du Sert N, Ahluwalia A, Alam S, Avey MT, Baker M, Browne WJ, et al. Reporting animal research: explanation and elaboration for the ARRIVE guidelines 2.0. *PLoS Biol* (2020) 18:e3000411. doi:10.1371/journal.pbio.3000411

31. Tai YC, Ruangma A, Rowland D, Siegel S, Newport DF, Chow PL, et al. Performance evaluation of the microPET focus: a third-generation microPET scanner dedicated to animal imaging. *J Nucl Med* (2005) 46:455–63.

32. Loening AM, Gambhir SS. AMIDE: a free software tool for multimodality medical image analysis. *Mol Imag* (2003) 2:131–7. doi:10.1162/153535003322556877

33. Logan J. Graphical analysis of PET data applied to reversible and irreversible tracers. *Nucl Med Biol* (2000) 27:661–70. doi:10.1016/s0969-8051(00)00137-2

34. Schneider D, Oskamp A, Holschbach M, Neumaier B, Bauer A, Bier D. Relevance of *in vitro* metabolism models to PET radiotracer development: prediction of *in vivo* clearance in rats from microsomal stability data. *Pharmaceuticals (Basel)* (2019) 12:57. doi:10.3390/ph12020057

35. Traxl A, Mairinger S, Filip T, Sauberer M, Stanek J, Poschner S, et al. Inhibition of ABCB1 and ABCG2 at the mouse blood-brain barrier with marketed drugs to improve brain delivery of the model ABCB1/ABCG2 substrate [(11)C]erlotinib. *Mol Pharmaceutics* (2019) 16:1282–93. doi:10.1021/acs.molpharmaceut.8b01217

36. Harada R, Okamura N, Furumoto S, Furukawa K, Ishiki A, Tomita N, et al. 18F-THK5351: a novel PET radiotracer for imaging neurofibrillary pathology in alzheimer disease. *J Nucl Med* (2016) 57:208–14. doi:10.2967/jnumed.115.164848

37. Waxman DJ, Holloway MG. Sex differences in the expression of hepatic drug metabolizing enzymes. *Mol Pharmacol* (2009) 76:215–28. doi:10.1124/mol.109.056705

38. Alzghool OM, Rokka J, Lopez-Picon FR, Snellman A, Helin JS, Okamura N, et al. (S)-[18F]THK5117 brain uptake is associated with Aβ plaques and MAO-B enzyme in a mouse model of Alzheimer's disease. *Neuropharmacology* (2021) 196:108676. doi:10.1016/j.neuropharm.2021.108676

39. Murugan NA, Chiotis K, Rodriguez-Vieitez E, Lemoine L, Agren H, Nordberg A. Cross-interaction of tau PET tracers with monoamine oxidase B: evidence from *in silico* modelling and *in vivo* imaging. *Eur J Nucl Med Mol Imaging* (2019) 46:1369–82. doi:10.1007/s00259-019-04305-8

40. Saura J, Richards JG, Mahy N. Differential age-related changes of mao-a and mao-b in mouse brain and pe peripheral organs. *Neurobiol Aging* (1994) 15:399–408. doi:10.1016/0197-4580(94)90071-x

41. Carter SF, Scholl M, Almkvist O, Wall A, Engler H, Langstrom B, et al. Evidence for astrocytosis in prodromal Alzheimer disease provided by 11C-deuterium-L-deprenyl: a multitracer PET paradigm combining 11C-Pittsburgh compound B and 18F-FDG. *J Nucl Med* (2012) 53:37–46. doi:10.2967/jnumed.110.087031

42. Sanfilippo C, Castrogiovanni P, Imbesi R, Lazzarino G, Di Pietro V, Li Volti G, et al. Sex-dependent monoamine oxidase isoforms expression patterns during human brain ageing. *Mech Ageing Dev* (2021) 197:111516. doi:10.1016/j.mad.2021.111516